A novel contact interaction formulation for voxel-based micro-finite-element models of bone

P. Bhattacharya[1,2]*, D. Betts[3] and G. H. van Lenthe[1]

[1] *KU Leuven – University of Leuven, Department of Mechanical Engineering, Biomechanics Section, Celestijnenlaan 300C, bus 2419, 3001 Leuven, Belgium*

[2] *Insigneo Institute for* in silico *Medicine and Department of Mechanical Engineering, University of Sheffield, Pam Liversidge Building, Mappin Street, Sheffield S1 3JD, United Kingdom*

[3] *ETH Zürich, Institut für Biomechanik, HCP H 22.2, Leopold-Ruzicka-Weg 4, 8093 Zürich, Switzerland*

SUMMARY

Voxel-based micro-finite-element (μFE) models are used extensively in bone mechanics research. A major disadvantage of voxel-based μFE models is that voxel surface jaggedness causes distortion of contact-induced stresses. Past efforts in resolving this problem have only been partially successful; i.e., mesh smoothing failed to preserve uniformity of the stiffness matrix, resulting in (excessively) larger solution times, whereas reducing contact to a bonded interface introduced spurious tensile stresses at the contact surface. This paper introduces a novel 'smooth' contact formulation that defines gap distances based on an artificial smooth surface representation while using the conventional penalty contact framework. Detailed analyses of a sphere under compression demonstrated that the smooth formulation predicts contact-induced stresses more accurately than the bonded contact formulation. When applied to a realistic bone contact problem, errors in the smooth contact result were under 2%, whereas errors in the bonded contact result were up to 42.2%. We conclude that the novel smooth contact formulation presents a memory-efficient method for contact problems in voxel-based μFE models. It presents the first method that allows modeling finite slip in large-scale voxel meshes common to high-resolution image-based models of bone while keeping the benefits of a fast and efficient voxel-based solution scheme. Copyright © 2010 John Wiley & Sons, Ltd.

Received . . .

Prepared using nmeauth.cls

DOI: 10.1002/nme

INTERNATIONAL JOURNAL FOR NUMERICAL METHODS IN ENGINEERING

Int. J. Numer. Meth. Engng 2010; **00**:2–??
KEY WORDS: Solids; Finite element methods; Micro-finite element analysis (μFEA); Voxel-based models; Bone biomechanics; Contact stress
Published online in Wiley InterScience (www.interscience.wiley.com). DOI: 10.1002/nme

1. INTRODUCTION

Micro-computed-tomography (μCT) images of bone, discretized on a Cartesian grid, can be used directly to define a micro-finite-element (μFE) model where each volume element (henceforth voxel) has an identical cubic shape. Over the last three decades, voxel-based μFE models have been used to perform non-invasive biomechanical investigations [1, 2, 3]. Recent advances in using highly-parallelized multi-grid solvers have made it possible to rapidly solve voxel-based μFE models with millions of degrees of freedom (DOFs) [4]. The advent of voxel-based μFE models have not only revolutionized healthcare technology at the point-of-care (e.g. HRpQCT-based bone strength analysis [5]) but have also pushed the frontiers of exploitation of imaging techniques (Synchrotron Radiation CT-imaging [6]). Voxel-based μFE modelling is perhaps indispensible in studying bone-remodelling within cancellous tissue since it possesses the necessary level of microstructural fidelity in comparison to homogenized continuum FE models [7, 8].

In voxel-based μFE models all voxel edges are oriented along the same Cartesian axes. These models fail to smoothly discretize any surface that has an orientation different from the three Cartesian directions. A natural surface, e.g., of a bone, thus becomes jagged in the voxel representation and causes artificial stress and traction concentrations. To overcome this problem, researchers have investigated the effect of smoothing the surface by distorting the voxels [9, 10, 11, 12]. Using a model of a two-dimensional (2D) annular ring it has been shown that smoothing, but not mesh refinement, reduces the error in the predicted stresses [11]. However, mesh smoothing increases computing costs as the stiffness matrix for each distorted element must be computed individually. For example, in a model of trabecular bone microstructure the application

*Correspondence to: Insigneo Institute for *in silico* Medicine and Department of Mechanical Engineering, University of Sheffield. Pam Liversidge Building, Mappin Street, Sheffield S1 3JD, United Kingdom. E-mail: p.bhattacharya@sheffield.ac.uk. Phone: +44 114 222 6174.

of smoothing to voxel-based meshes did not result in a significant reduction of stresses on the bone surfaces compared to the substantial increase in simulation times [9, 10].

For problems involving contact, the error is further influenced by a modelling artifact related to the orientation of the voxel relative to the loading direction [13]. Quantification of the contact-induced errors in stress prediction accounting for voxel orientation, is yet to be performed. The error in the predicted stress at the boundary becomes critical in models where contact is present. A common approach is to 'bond' the opposing surfaces [14, 15, 3, 16]. By design, this method is not suitable in situations where node contact pairs are changing during the simulation: e.g. incipient contact, secondary instability and finite sliding. Hence, this bonding approach has been restricted to some limited scenarios of loading at the bone–implant interface. Though the global strength [3] and apparent stiffness [14] of the bone–implant bond have been satisfactorily predicted by this approach, the quality of local stress prediction remains unknown. Furthermore, tensile tractions can be predicted which obviously cannot occur in physical reality.

In standard FE, the node-to-surface contact formulation [17, 18] has been widely used to model three-dimensional (3D) contact interaction. In this formulation, one of the two contacting surfaces (the 'master' surface) possesses a higher stiffness, lower mesh refinement, lesser degrees of freedom, or a combination of these, compared to the opposing ('slave') surface. The orientation of voxels edges and the shape of the voxels at the slave surface do not influence the contact formulation. Only the separation distance of slave-surface nodes relative to the master surface elements determines the contact stresses.

The aim of this paper is to develop an efficient contact algorithm that can take full advantage of voxel-based meshes. We hypothesize that the contact-induced stresses can be quantified using the penalty-based contact formulation from standard FE, while redefining the distance between slave nodes relative to the master surface based on an artificially defined surface that does not alter the shape of the voxels. The paper introduces a 'smooth' contact formulation in which the node-to-surface formulation is modified by defining ghost slave nodes that lie on a nominally smooth surface. The novelty of this approach is that the problem of accurate contact stress prediction is

DOI: 10.1002/nme

separated from the problem of maintaining the homogeneity of the voxelated geometry. The ghost slave nodes are used to calculate gap distances which ensure correct contact stresses. On the other hand, the voxelated nature of the elements ensures that fast and highly memory efficient solvers can be used. The problem of elastic compression of a sphere is analyzed using voxel-based models. This problem is the 3D counterpart of the elastic compression of an infinitely long cylinder in 2D [19, p. 107]. The sphere model allows the investigation of contact-induced errors in dependence of mesh refinement and relative voxel orientation without other confounding factors. The effectiveness of the novel smooth contact formulation is demonstrated further by analysing the problem of contact in a human hip joint between the femur and the acetabulum, which is more realistic than the problem of elastic compression of a sphere.

2. METHOD

2.1. Finite-element discretization and contact formulations

In the standard FE approach [18, 20, 21] a contact problem is expressed by the matrix equation

$$0 = \mathbf{F} + \mathbf{R}^c - \mathbf{K}\mathbf{a} \tag{1}$$

where $\mathbf{K}$ is the stiffness matrix, $\mathbf{F}$, $\mathbf{R}^c$ and $\mathbf{a}$ are the vectors of applied forces, contact forces and nodal displacements, respectively. In the penalty contact enforcement method, the contact force $\mathbf{R}^c$ is related to the contact gap between the opposing contact surfaces through a contact-interaction law. For example, a hard–frictionless contact is specified as

$$\mathbf{R}^c = \begin{cases} -k_c g_n \mathbf{n} & g_n < 0 \\ 0 & \text{otherwise} \end{cases} \tag{2}$$

Here a node-to-surface discretization is used, with one contact surface defined as the master and the opposite surface defined as the slave. The contact force acting on any node of the slave surface is given by $\mathbf{R}^c$ above, k_c is a constant scalar referred to as the penalty stiffness parameter, the contact gap is defined as $g_n \equiv \mathbf{n} \cdot (\mathbf{s} - \mathbf{m})$, $\mathbf{n}$ is the current outward normal to the master facet closest to the slave node, $\mathbf{s}$ is the current position of the slave node and $\mathbf{m}$ is the current position of a node on the

DOI: 10.1002/nme

closest master facet. Equal and opposite contact forces are distributed on nodes of the master facet. For nodes that do not belong to either the master or slave surfaces, the contact force is zero.

The set of equations (1) and (2) is non-linear in $\mathbf{a}$, since $\mathbf{R}^c$, g_n and $\mathbf{n}$ depend on $\mathbf{a}$ through their dependence on current nodal positions. To determine the unknowns $\mathbf{a}$ and $\mathbf{R}^c$, one attempts to iteratively minimize the residual

$$\mathbf{r} = \mathbf{F} + \mathbf{R}^c - \mathbf{K}\mathbf{a} \tag{3}$$

Using Δ to denote a variation between successive iterations, linearization of Eqs. (2) and (3) gives

$$\Delta\mathbf{R}^c = -\mathbf{K}^c\Delta\mathbf{a} \tag{4}$$

$$\Delta\mathbf{r} = \Delta\mathbf{R}^c - \mathbf{K}\Delta\mathbf{a} \tag{5}$$

where $\mathbf{K}^c$ is the so-called contact stiffness matrix. The displacement update that minimizes the residual (i.e. $\mathbf{r} + \Delta\mathbf{r} = 0$) is obtained by combining Eqs. (3)–(5), to get

$$\Delta\mathbf{a} = (\mathbf{K} + \mathbf{K}^c)^{-1}(\mathbf{F} + \mathbf{R}^c - \mathbf{K}\mathbf{a}) \tag{6}$$

The updates are iteratively computed and applied to $\mathbf{a}$ until convergence is reached. This conventional formulation is henceforth referred to as the Stair-Case, Sliding Contact (SC-SC) model, where ‘stair-case’ highlights the jaggedness of the voxelated slave surface, and ‘sliding contact’ highlights that slave node displacement tangential to the master surface is not restricted. We note that the entire treatment is a standard approach and has been discussed in detail in textbooks on the subject [18].

In the smooth contact formulation, each slave node is identified with a ghost slave node, where the ghost slave nodes lie on a smooth representation of the voxelated slave surface in the reference configuration. It is not needed to discretize the smooth representation of the voxelated surface into finite surface elements, and one may identify the ghost slave node as the position on the smooth representation of the voxelated surface that is closest to the slave node in the SC-SC model. Identical displacements are applied to the slave node and its corresponding ghost slave node at all times. The only difference in the smooth contact formulation with respect to the SC-SC model is that the contact gap is redefined as $g_n \equiv \mathbf{n}\cdot(\tilde{\mathbf{s}} - \mathbf{m})$ where $\tilde{\mathbf{s}}$ is the ghost slave node position in the current configuration. This redefinition modifies the computed contact force vector $\mathbf{R}^c$ and the contact stiffness matrix $\mathbf{K}^c$, but only up to their dependence on the contact gap distance g_n. This smooth contact formulation is henceforth referred to as the Simulated Smoothed surface, Sliding Contact (SS-SC) model. 'Simulated smoothed surface' highlights that ghost slave nodes lying on a fictitious smooth surface are employed in defining the gap distance, but also that this redefinition is the only difference with respect to the SC-SC model. In particular, the voxels connected to slave nodes are not deformed, and the stiffness matrix $\mathbf{K}$ is identical for the SC-SC and SS-SC formulations. The novelty of our method is that an artificial surface is defined that is used to calculate gap distances while the voxelated nature of the elements is kept such that fast and highly memory efficient solvers can be used.

3. APPLICATION TO ELASTIC COMPRESSION OF A SPHERE

Consider a deformable sphere (radius R) with its centre at the origin O. In the reference configuration the sphere is stress-free and positioned between two parallel rigid planes that are touching the sphere. We consider the problem where the distance between the rigid planes reduces by $0.2R$ leading to 10 % apparent compressive strain in the sphere.

3.1. Voxel models

Define a rectangular coordinate system (x, y, z) with the origin located at O and with the direction x aligned along the sphere diameter normal to the rigid contact planes. A reduced form of the above problem is considered by noting that irrespective of the choice of voxelation procedure, the problem is symmetric about the equatorial plane $x = 0$. Hence only the hemispherical region and the one rigid plane lying in the half-space $x \geq 0$ is considered. In this reduced model the surface of the hemisphere initially at $x = 0$ always remains planar but displaces a distance of $0.1R$ in the $+x$-direction. The rigid plane is held fixed in space.

The hemispherical volume is populated by 8-noded linear voxels (side length $a < R$) with edges aligned to a coordinate system (X, Y, Z) with origin at O. The choice of X, Y and Z directions is made as follows. We note that the orientation of the voxels of the hemisphere relative to the rigid contact plane is determined by the orientation of the (X, Y, Z) system relative to the (x, y, z) system. However, due to cubic symmetry of the voxels, only part of the voxelated hemisphere boundary presents unique voxel orientations to a locally tangent plane (shaded region in Figure 1A). It is easy to see that in two dimensions this is equivalent to the fact that only a 45° sector of a pixelated circle presents unique orientations to a locally tangent segment (Figure 1B). Hence locations labeled Loc-1 to Loc-7 are identified within the shaded region (Figure 1A) in order to investigate contact-induced errors in dependence of relative voxel orientation. Coordinates of these locations in the (X, Y, Z) system are listed in Table I. The directions of the coordinate axes (X, Y, Z) are selected such that the locations Loc-i ($i = 1 \ldots 7$) in the (X, Y, Z)-system corresponds to the location $(R, 0, 0)$ in the (x, y, z)-system and the Y axis lies anywhere on the x–y plane.

Voxelating the hemisphere in the above manner ensures that all voxels possess at least one node for which $x \geq 0$. A flat equatorial surface is obtained by setting $x = 0$ for nodes with $x < 0$. To model the rigid contact plane, a 4-noded rectangular surface element is defined with nodes located at $x = R + g_0$, $y = \pm 0.5R$, $z = \pm 0.5R$. The nominal gap $g_0 = 2a$ between the hemisphere and the rectangular element ensures that penetration does not occur in the reference configuration, irrespective of the choice of voxel size and orientation. In all, 49 different voxel geometries are analysed. In these models the relative orientation between (X, Y, Z) and (x, y, z) coordinate systems varies from Loc-1 to Loc-7 and mesh refinement a/R varies as 0.01, 0.0125, 0.025, 0.0375, 0.05, 0.075 and 0.1 (Figure 2).

In all models the hemisphere is considered to be homogeneous isotropic linear elastic with Young's modulus $E = 10$ GPa and Poisson's ratio $\nu = 0.3$. To achieve 10% apparent compressive strain, all nodes of the hemisphere located at $x = 0$ in the reference configuration are displaced by $0.1R + g_0$ in the $+x$-direction. The y- and z-degrees of freedom (DOFs) of the node at O and the z-DOF of the node nearest to $(0, 0.5R, 0)$ are constrained throughout the solution, thus restricting rigid-body translation and rotation. All nodes of the rectangular surface element are held fixed in space. The total displacement is applied over 10 equal increments.

Nodes on the hemisphere surface with $x > 0.9R$ are defined as slave nodes. To simulate bonded contact, all degrees of freedom are restricted for all the slave nodes. For SS-SC models, each slave node position in the reference configuration is projected in the radial direction on the surface of the analytical hemisphere to obtain the corresponding ghost slave node position in the reference configuration. For both SC-SC and SS-SC, hard–frictionless contact interaction is modelled between slave nodes and the master surface (rectangular surface element). The penalty contact stiffness parameter is taken to be $k_c = 0.1ER$ for all models and this was found to result in negligible overclosure. Contact iterations are assumed to have converged if either the maximum absolute difference in nodal displacements between the current contact iteration and the last contact iteration is less than 0.01% of the maximum absolute difference in nodal displacements between the current contact iteration and the last converged increment, or a maximum 10 contact iterations have been performed. The FE models are analyzed using an in-house FE code developed and executed with MATLAB version 8.5.0 (R2015a) (The Mathworks Inc., Massachusetts, United States). Computed results are visualized using software ParaView version 4.3.1 (Kitware Inc., New York, United States).

3.2. Benchmark model

The benchmark model of the problem is created using a geometry conforming mesh. Axisymmetry reduces the problem to a plane of revolution (Figure 3). The centre of the sphere O coincides with the origin of the planar coordinate system (ξ, ρ). The axis of revolution is ξ and only the quadrant $\xi, \rho \geq 0$ is considered.

The 2D domain of the hemisphere cross section is meshed using 4-noded linear axisymmetric elements with increasing refinement closer to the contact region (element size $\sim 0.005R$). The rigid contact plane is represented by a line segment parallel to the ρ axis and passing through $(R, 0)$. The contact line segment is treated as an analytical solid and is thus not discretized. In the reference configuration the hemisphere and the rigid plane are just in contact.

The hemisphere possesses identical constitutive behavior as the voxel-based models. To achieve 10% apparent compressive strain, the nodes at the top of the hemisphere are given a displacement of $0.1R$ in the $+\xi$-direction, while nodes situated on the ξ-axis are constrained from movement in the ρ-direction. The contact line segment is held fixed in space. Hard–frictionless contact behavior using penalty contact enforcement method is implemented using the node-to-surface formulation and with the identical numerical value for k_c as in the voxel models. The hemisphere boundary nodes are defined as slave nodes and the contact line segment acts as master surface. The model is solved using software Abaqus/Standard version 6.13-1 (Dassault Systèmes Simulia Corp., Rhode Island, United States).

4. APPLICATION TO THE HUMAN HIP JOINT

Grosland et al. [22] considered the problem of compressive contact at the human hip joint between the femur and the acetabulum. In this paper we considered the same problem, except that: (a) bone geometries are taken from the public data repository of the VAKHUM project [23, 24], (b) a smaller subset of the proximal femur volume is analyzed, (c) a displacement-control boundary condition is applied to the femur (instead of a load-control boundary condition being applied to the pelvis), and (d) the meshing and contact interaction details are as described below. Stereolithography (STL) files for the segmented surfaces of a left femur and a pelvis were downloaded from the repository. Only a subset of the pelvis STL in the region near the acetabulum are retained (61801 facets attached to 33477 nodes). The STL for the femur is also cropped to retain triangular facets only in the head region. Additional geometric features (edges and surfaces) are generated to define a closed volume of the femoral head region. Following Grosland et al. [22], a rigid–deformable contact scenario is considered, whereby the pelvis is considered a rigid body and the femur is deformable. Pelvis STL facets are directly used for the surface definition and no volume mesh or material definitions are added. In the reference configuration the femur and pelvis regions do not inter-penetrate and the average contact gap in the acetabular region is ~ 1.5 mm.

Prepared using nmeauth.cls

DOI: 10.1002/nme

4.1. Voxel models

The voxel model for the above problem is created as follows. The image data from the VAKHUM dataset used a reference coordinate system in which the axes were aligned nominally with the anatomical body axes. The same rectangular coordinate system is used here, hence the x, y and z directions are parallel to the medial–lateral, anterior–posterior and inferior–superior directions respectively. The closed volume of the femur head is discretized using a freely available mesh voxelation package [25]. A total of 55962 linear voxels (side length 1 mm) and 61832 nodes are generated. All voxels possessed linear isotropic elastic material properties ($E = 10$ GPa, $\nu = 0.3$). A displacement, with medial and superior components equal to 3 mm, is applied to all nodes on the lateral and inferior planar surfaces of the femur. For one node on each of these two surfaces, the anterior–posterior displacement component is set to zero in order to prevent spurious rigid body motion.

In the bonded contact model, the pelvis STL is used to identify a subset of the femur surface nodes which are to be 'bonded'. Specifically, femur surface nodes within $3\sqrt{2}$ mm (= magnitude of applied displacement) of the nearest pelvis facet in the reference configuration are selected. Once these 'bonded' nodes are identified, the pelvis geometry is discarded, and the 'bonded' nodes are held fixed for the rest of the analysis. The displacement of the lateral and inferior planar surfaces of the femur is applied over a single increment.

In the SC-SC model, all pelvis facet nodes are held fixed in space. Hard-frictionless contact behavior using a node-to-surface discretization is defined between the femur and the pelvis models. All facets of the pelvis models are considered to be potential master surface facets. Exterior nodes of the femur voxel mesh that are on the acetabulum-facing side of a plane (Figure 4) are defined as slave nodes because only these are likely to come into contact. In the SS-SC model, ghost slave node positions in the reference configuration are defined by projecting the slave nodes of the SC-SC model on to the nearest facet of the femur STL. The total displacement of the femoral head is applied over 5 equal increments. Within each increment, contact is considered between a slave node/ghost slave node (SC-SC/SS-SC) and all those master facets which have at least one node within 4 mm

DOI: 10.1002/nme

of the current slave node/ghost slave node position. A penalty contact stiffness of $k_c = 1$ GPa.mm was found to result in negligible overclosure. Contact iterations are assumed to have converged if either the maximum absolute difference in nodal displacements between the current contact iteration and the last contact iteration is less than 0.01% of the maximum absolute difference in nodal displacements between the current contact iteration and the last converged increment, or if a maximum 10 contact iterations have been performed. All voxel models are analysed using the in-house finite-element code noted previously.

4.2. Benchmark model

The coordinate axis system of the benchmark model is identical to that of the voxel models. A tetrahedral mesh is used to discretize the femur head volume using Ansys ICEM CFD 15.0 (ANSYS Inc., Pennsylvania, United States) thus generating 137854 nodes and 788620 linear tetrahedra (nominal element size 1 mm). The triangulated pelvis surface possessed the same rigid body definition as in the voxel models.

The femur volume is given identical material properties as in the voxel models. The boundary conditions applied on the femur and pelvis are identical to that in the voxel models. General contact interaction (surface-to-surface contact formulation) is defined between all surface elements of the femur and the pelvis models. Hard–frictionless contact behavior is simulated using the penalty method and an identical value of penalty stiffness k_c as in the voxel models. The benchmark model is solved incrementally, with the total displacement being applied over 5 equal increments. The model is analysed using Abaqus/Standard.

4.3. Analysis

Computed results are visualized using ParaView. Qualitative comparison of contact-induced stresses between the benchmark and the voxel models is performed by considering stress distributions on a coronal plane of the femoral head plotted in the undeformed configuration. Quantitative comparison of the voxel models with respect to the benchmark model is performed by considering all voxel nodal locations.

DOI: 10.1002/nme

5. RESULTS

5.1. Elastic compression of sphere

As an illustrative result, in Figure 5 the minimum principal stress contours (normalized by E) are plotted on the $y = 0$ plane (reference configuration) for the bonded, SC-SC and SS-SC models, for a representative mesh refinement and voxel orientation ($a/R = 0.075$, Loc-1). In the bonded model, the peak compressive stress occurs at the corners of the bottom-most voxels. This peak compressive stress is also significantly larger in magnitude than the peak compressive stress in the SC-SC and the SS-SC models. Although the peak compressive stress magnitudes are similar in the SC-SC and SS-SC models, the location of the peak compressive stress is more realistic for the SS-SC model than in the SC-SC model. Thus for this representative case, the bonded model predicts both the location and the magnitude inaccurately, the SC-SC model predicts the location inaccurately, while the SS-SC model performs the best of all three.

Now considering the results in more detail, stresses and distances are normalized by E and R respectively. Results are reported as a function of the distance along the x (or ξ for benchmark) axes in the undeformed configuration. The normalized distances 0 and 1 correspond respectively to the hemisphere center and the point of nominal contact initiation $(R, 0, 0)$. Figure 6A shows all three principal stresses in the benchmark model. The highest compressive stress at any point, and thereby the minimum principal stress direction, is expectedly along x which is the direction of loading. The middle and the maximum principal stresses at any point (Figure 6A) are identical as a consequence of axisymmetry. For the sake of brevity, mid-principal stresses are omitted from further analysis. In the region $x/R \lesssim 0.63$ the maximum principal stress is tensile due to the Poisson's effect in which compression along x causes a radially outward stretch in the y–z plane. Figures 6B, C compare the maximum and minimum principal stresses respectively between the benchmark and the voxel models with $a/R = 0.075$ and orientation Loc-1. The maximum principal stress in these particular voxel models compares better with the benchmark than the minimum principal stress. The maximum error in any contact formulation is expectedly the largest at the point of contact. The magnitude of this largest error is nearly the same for the bonded and SC-SC formulations, and is minimized for SS-SC.

In the following we focus on the region close to the contact surface ($x/R \geq 0.8$). Figure 7 considers principal stresses in dependence of orientation and contact formulation for the coarsest ($a/R = 0.1$) and the most refined ($a/R = 0.01$) mesh models. The dispersion across the different voxel orientations reduces as the mesh is refined irrespective of the choice of contact model. As the mesh is refined, variation reduces at nearly every location along the radial line, along with a reduction in extent of the region of large variations. The overall variation in minimum principal stress is larger than the variation in maximum principal stress for all contact models. For the bonded contact formulation (Figure 7A, D) the average error, i.e. the difference between the centerline of the dispersion envelope and the benchmark, does not change significantly due to mesh refinement. This result is true for either principal stress. For SC-SC (Figure 7B, E) the average errors are significantly reduced compared to bonded contact, and the reduction is higher for the most refined mesh models. Yet, the maximum widths of the dispersion envelopes, which occur close to the point of contact, are substantially larger in SC-SC compared to those in bonded contact for both mesh refinements. Thus, going from bonded to SC-SC, the accuracy is improved, but the precision is poorer. In contrast, when SS-SC is used (Figure 7C, F), both the average error and the maximum dispersion are reduced compared to bonded contact – irrespective of mesh refinement or principal stress being considered. Thus both accuracy and precision improve in SS-SC when compared to bonded contact. Increasing mesh refinement leads to an increase in accuracy everywhere, but precision increases nearly everywhere except in a very small region close to contact.

Next, for each principal stress component the normalized maximum absolute error (NMAXABSE) was quantified as a local error measure:

$$\mathrm{NMAXABSE} = \frac{\max\limits_{i \in [1,N]} |\sigma_i - \tilde{\sigma}_i|}{\max\limits_{i \in [1,N]} |\sigma_i|} \tag{7}$$

DOI: 10.1002/nme

For each stress component the normalized root mean square error (NRMSE) was defined as a global error measure as follows:

$$\mathrm{NRMSE} = \frac{\sqrt{\operatorname*{avg}_{i\in[1,N]} (\sigma_i - \tilde{\sigma}_i)^2}}{\max_{i\in[1,N]} |\sigma_i|}. \tag{8}$$

where σ and $\tilde{\sigma}$ are the principal stress variable obtained from the benchmark and a voxel-based model respectively. The subscript i is the index of $N = 100$ equispaced points along $x/R \geq 0.8$ where the stresses are evaluated. The normalization factor in the denominator is effectively the value of the principal stress variable at the point of contact.

For a specific combination of mesh refinement, contact model and principal stress variable, both NMAXABSE and NRMSE depend on voxel orientation. We assume that for an arbitrary orientation the predicted stress would lie wholly within the envelope of predicted stress values corresponding to the seven orientations considered here. With this assumption we obtain the maximum and minimum values of NMAXABSE and NRMSE across all orientations. A larger difference between the maximum and minimum values is taken to render the local (NMAXABSE) or global (NRMSE) prediction less precise. A larger average of the maximum and minimum values is taken to render the local or global prediction less accurate. For the bonded contact models, considering any principal stress, no significant change in local precision or local accuracy is observed as a function of mesh refinement (Figures 8A,D). At any given refinement, local precision and local accuracy are similar between maximum and minimum principal stresses.

For SC-SC models (Figures 8B,E), considering any principal stress, mesh refinement does not improve the local precision, but local accuracy increases for maximum principal stress while it remains nearly unchanged for minimum principal stress. Minimum principal stress predictions are less accurate and less precise locally than maximum principal stress predictions for a given refinement. Comparing with bonded contact, the local accuracy in SC-SC is higher for both principal stresses at any given mesh refinement. However, the local precision is poorer in SC-SC than in bonded contact, and especially so in the case of the minimum principal stress.

For SS-SC models (Figures 8C,F), considering any principal stress, mesh refinement does not change the local precision, but local accuracy increases for both principal stresses. At any given refinement, local precision and local accuracy are similar between maximum and minimum principal stresses. Comparing with bonded contact, local accuracy is higher in SS-SC for both principal stresses at any given mesh refinement. Most importantly, this improvement does not adversely affect local precision, which is similar between SS-SC and bonded contact for both principal stress.

All the above trends hold when considering global accuracy and precision. We draw attention to the fact that for a given combination of mesh-refinement, contact model and principal stress, both accuracy and precision are higher globally than locally. This highlights that the errors in predicted stresses are localized to the near-contact region.

5.2. *Femur–acetabulum contact*

Figure 9 compares the principal stress distribution on a coronal plane between the benchmark, bonded, SC-SC and SS-SC models. The errors in the bonded contact results compared to the benchmark model are substantial and even qualitative agreement is not achieved. Qualitatively, the SC-SC and the SS-SC results agree with the benchmark; but quantitatively, the SS-SC results are superior to the SC-SC results. For example, in the SC-SC results compressive stresses (negative value contours) are concentrated at corners of the boundary, an artifact that is avoided in the SS-SC results. Similarly, regions of negative valued principal stress contours are larger in SC-SC results than in the benchmark and the SS-SC results. This improves both near-surface and interior stress predictions for the SS-SC formulation compared to the SC-SC formulation.

The local (NMAXABSE) and global (NRMSE) accuracy in the prediction of principal, normal and shear stresses are compared between the different contact formulations in table II. These error measures were defined previously in Eqs. (7) and (8). For the hip contact problem, the stresses are evaluated at $N = 56313$ points, indexed $i = 1 \ldots N$, in the interior of the voxel models and the benchmark model. These points correspond to nodal positions of the voxel models. Due to differences in discretization between the voxel models and the benchmark model, $5519(= 61832 - 56313)$ voxel nodal positions fall outside the femoral volume of the benchmark model, and are omitted from the error analysis. Although only one voxelation direction was considered, it is noted that the relative orientation of the femur voxel edges and the pelvis facets varies over a large range of angles. This is a result of the highly conforming contact situation that naturally arises in this realistic problem. Hence, unlike in the sphere contact problem, the results here are not expected to change significantly with voxelation direction. It is found that the local accuracy increases going from SC-SC to SS-SC formulations for most stress invariants and components. The local accuracy for bonded contact is always and significantly worse than that for SS-SC. Global accuracy increases by an order of magnitude going from bonded contact to SC-SC, and by yet another order of magnitude when using SS-SC formulation. This highlights that the errors in predicted stresses are spread throughout the femoral head volume. For all the stress variables considered, global errors are up to 42.2% for the bonded model, but only up to 1.16% for the SS-SC model.

6. DISCUSSION AND CONCLUSIONS

The jagged surface nature of voxel-based FE models prevents an accurate determination of stresses for a body in contact. Considering first the simple problem of elastic compression of a sphere, it was shown that voxel models exhibited spurious stress concentrations at and near the region of contact. Errors were found to depend on voxel orientation, mesh refinement, choice of contact model and stress variable itself. With increasing mesh refinement, the accuracy of stress prediction was unchanged for bonded contact. Compared to the bonded contact results, accuracy was higher for both SC-SC and SS-SC, and even improved in general with increasing mesh refinement. However, SS-SC performed significantly better than SC-SC in increasing the precision across voxel orientations. The precision in SC-SC was similar or worse than that in bonded contact, and remained nearly unchanged with increasing mesh refinement. In a strong contrast, the precision in SS-SC was similar or smaller than that in bonded contact, and decreased with increasing mesh refinement. Thus the advantage of mesh refinement is expected only in the presence of SS-SC.

In the present study, the most refined voxel model ($a/R = 0.01$) with mesh orientation Loc-1 comprised $\sim$ 6.6 million DOFs. In terms of absolute size of model, this compares to models solved

DOI: 10.1002/nme

with specialized voxel-based FE codes, but is smaller than what these dedicated solvers can handle (up to problems with $\sim$ 500 million DOFs [4, 26, 27]). Yet, it should be noted that the appropriate parameter for estimating contact error is the ratio a/R, and not the absolute number or size of the voxels. In bone research, the development of newer imaging devices (from QCT to HRpQCT to μCT), has come with an increase in resolution, with smaller voxel dimensions and increasing size of the models. At the same time the radius of curvature R of the bone surface also decreases as bone/non-bone regions are better distinguished with increasing resolution. Hence, in continuum-FE models, a is typically $\sim O(1\ \text{mm})$ [28, 29, 30] and R is of the order of the whole bone dimension. Considering the diameter of a vertebra, radius or femoral head, here $R \sim O(10\ \text{mm})$ [30, 31] and $a/R \sim 0.1$. In μFE models, a is typically $\sim O(50\ \mu\text{m})$ [32, 33, 34] and R is of the order of the largest microstructural feature. Considering trabecular separation as the largest feature, here $R \sim O(1\ \text{mm})$ [35] and $a/R \sim 0.05$. For typical models reported in the literature and that were executed using state-of-the-art FE codes [32, 33, 34, 28, 29, 30], it was always found that $a/R > 0.03$, irrespective of whether μFE or continuum-FE models were analysed. Hence, the smallest ratio used in the present study ($a/R = 0.01$) is substantially smaller (i.e., better) than those for models presented in the literature. In addition to this, for the range of refinements considered in the present study, the differences in precision and accuracy between SS-SC model on one hand, and either Bonded contact model or SC-SC model on the other, show strongly asymptotic trends. These facts strongly emphasize that mesh refinement cannot be expected to improve the performance of either the Bonded contact model or SC-SC model vis-à-vis the SS-SC model.

In the human hip joint contact problem, the femoral head had an overall radius of curvature of about 25 mm, but possessed some local features with radii of curvature down to about 5 mm (visual estimates). Additionally, in this problem nearly all possible voxel orientations relative to the pelvis contact surface were realized due to the highly conforming contact situation. In light of the sphere-compression results, voxel models of the femur–acetabulum problem, created with side length 1 mm ($a/R \sim 0.04$ for the whole femoral head), were expected to show significant errors in bonded contact prediction especially at the near-surface regions. For the SC-SC and SS-SC models

Prepared using nmeauth.cls

DOI: 10.1002/nme

relatively smaller errors were expected, with additional quantitative improvement expected for SS-SC due to the lower dispersion in errors. However, close to the local features of high curvature (where $a/R \sim 0.2$), it was expected that the errors in all contact models would be similar and high. Yet, the prediction of the stress distributions throughout the femoral head interior by the SS-SC formulation was found to be excellent, and was better than that by the SC-SC and bonded contact formulations. This can be explained by the fact that the contact-induced stresses in the hip joint problem influenced a much larger region around the points of contact than in the sphere compression problem, leading to suppression of localized regions of large error. The benchmark results show that the influence of contact was evident even at significant depths from the femoral head surface. This explains why the relative performance improvement in the SS-SC formulation compared to the SC-SC formulation (as evidenced by the global quantity NRMSE) was even better than that estimated by the sphere compression results. The results from the bonded contact model, which represents the state-of-the-art in μFE, was found to be of very low quality throughout for this particular problem. The inability to allow finite slipping led to tensile stresses at the contact boundary.

In the SC-SC and SS-SC models, the subset of slaves nodes that participate actively in contact (i.e. possess a non-zero contact force magnitude) emerge automatically during the solution procedure. Hence, considering a larger set of nodes as slave nodes initially does not affect the end result. This is not the case for the bonded contact approach, as too many bonded nodes would cause larger deviations in the result. In order not to artificially bias against the bonded result in this manner, we selected the bonded nodes based on the initial gap distance between the femur and the pelvis. This set of nodes was a smaller subset of the set of nodes defined as slave nodes in the SC-SC and SS-SC femur models. In order to test that this subset was not too small, i.e. it did not omit locations that would otherwise participate in contact, we analysed the SC-SC and SS-SC results *a posteriori*. It was found that the slave nodes that were in active contact were a subset of the nodes defined as bonded nodes, thereby assuring that the bonded model did not bond too few nodes.

Contact stress concentrations due to voxel-based meshes are a numerical artefact, and arise due to the approximation of a nominally smooth ‘real’ physical surface with jagged voxels. These

DOI: 10.1002/nme

stress concentrations are different in nature from contact stress concentrations that often arise due to local non-smoothness of the underlying real physical surface. This is well illustrated in the hip joint contact problem analysed in this paper. Contact stress concentrations appeared even in the benchmark model (where voxels are absent) such as underneath the 'bump' at the top of the femur head (Figure 9I). Stress concentrations due to the bump-like features can be reduced by adding a soft layer at the interface. Indeed, in reality, a thin, soft cartilage layer covers the femoral head surface and prevents such stress concentrations. However, even if such a layer is modelled, it cannot remove the stress concentrations due to voxelation. This is demonstrated by modifying the hip joint contact problem above by giving elastic properties [36] simulating cartilage ($E = 2$ MPa, $\nu = 0.3$) to elements within 2 mm [37] of the surface. In addition, to account stress heterogeneities in the thin cartilage layer, elements of 0.5 mm side length are used: in the benchmark model mesh, up to a depth of 4 mm from the surface; and in the voxel model mesh, everywhere. Both refinements ensure approximately 4 elements through the thickness of the cartilage layer (Figure 10A). Note that the 0.5 mm element size used in this modification is smaller than that used in the literature [30]. Under the predominantly compression loading scenario of the hip joint contact, the minimum principal stress σ_3 is the most important component of the stress response. Contours of σ_3 on a cross-section of the femoral head (with the cartilage layer present) are shown in Figure 10B. Comparing with Figure 9I–L, the cartilage layer is found to reduce as expected the stress concentrations in the near-surface region for all models by several orders of magnitude. However, for the voxel mesh models, irrespective of adding the cartilage layer the SS-SC model predicts σ_3 ($\mathrm{NMAXABSE} = 0.735,\ \mathrm{NRMSE} = 0.0337$) with higher accuracy (both local and global) than Bonded contact ($\mathrm{NMAXABSE} = 9.60,\ \mathrm{NRMSE} = 1.61$) or SC-SC ($\mathrm{NMAXABSE} = 0.787,\ \mathrm{NRMSE} = 0.0382$) models. It is to be noted that for each voxel model, both local and global errors increase when the cartilage layer is present than when it is not (c.f. Table II). This is perhaps because the increase in mesh refinement is not sufficient to match the decrease in the characteristic length of the solution introduced by the thin cartilage layer. The conclusions that can be drawn from this short study are as follows. For the purpose of reducing

DOI: 10.1002/nme

stress concentrations due to voxelation, a soft layer does not appear to be a better alternative to the SS-SC model. However, if a soft layer is included to simulate the physical reality better, the SS-SC model (with a global error less than 4%) is an excellent choice compared to Bonded contact model (where global errors exceed 150%).

The improvement in overall prediction accuracy going from the bonded contact model to the SS-SC model makes a strong case for why the latter should be implemented within state-of-the-art voxel-based μFE software. It is interesting to note that, to the best of our knowledge, no FE software package currently enables the customization of contact gap definition, i.e. the distance between a slave node and its corresponding master surface element. This definition is central to the SS-SC implementation, and its customizability should be considered in the design of contact analysis in FE software packages. In addition to specifying which nodes attached to the voxels are to be considered as slave nodes, the SS-SC model implementation requires a ghost slave node location (in the reference configuration) to be defined for each slave node. Typically, given a greyscale image stack and a threshold grey value, a voxel model can be generated by keeping only those points where the grey value is above/below the threshold. In such a voxel model, a set of surface nodes can be defined as slave nodes. At the same time, some form of the marching-cubes algorithm [38] can be used to obtain a triangulated surface mesh from the same greyscale image stack and the threshold grey value. Ghost slave nodes can be defined by simply finding a point on the triangulated surface nearest to each slave node. This straightforward procedure of defining ghost slave nodes was demonstrated by the hip contact problem analysed in this paper. As such, it can be applied to a large variety of biomedical geometries.

The present study has some limitations. The current implementation of the contact algorithm did not investigate the scenario when the master surface is deformable assuming it to be rigid in both the sphere compression and femur–acetabulum contact problems. This simplified the computation of the contact stiffness matrix terms since changes to the master surface normal could be neglected. In the application area of bone contact this assumption is reasonable, since the surfaces do not undergo large deformations and any rigid body motion can be removed by choosing the coordinate system to move with the master surface. However, numerical formulations of the additional contact stiffness matrix terms in the presence of a deformable master surface are readily found in the literature [18] and do not limit the implementation of the SS-SC formulation itself.

The constitutive behavior of the hemisphere and the femur were taken to be linear elastic homogeneous and isotropic. Past studies have shown that in the context of bone contact interaction, both elasticity and failure are important, and tension–compression non-linearity and anisotropy in both moduli and strength are expected to play a role. It is obvious that accounting for the above complexities will influence the accuracy and precision values estimated in this paper. Further studies are needed to evaluate the effect of such considerations on voxel-based contact analysis which were outside the scope of the present work.

In conclusion, a contact problem considered in this paper was that between a plane and a sphere, the latter possessing a homogeneous curvature at all points of its 3D surface. Use of this simple geometry removed confounding factors and enabled a thorough investigation of the effect of orientation and mesh-refinement on the accuracy of stress prediction. The superiority of the SS-SC formulation over the SC-SC and, in particular, the bonded contact formulations was shown to be valid across a range of values of orientation and mesh-refinement that is relevant to bone contact models. Subsequent to these findings, a realistic problem of femur–acetabulum contact was further investigated. It was found that the reduction in errors going from the SC-SC model to the SS-SC model was in fact much larger in this more realistic problem, than what was estimated from the sphere compression results. This can be explained by the inherent differences in how contact-induced stresses influence the solution between the realistic case and the simple problem. Furthermore, it was shown that the improvement due to the SS-SC algorithm over the state-of-the-art (bonded contact) was potentially even larger in realistic problems.

These findings demonstrate that the novel SS-SC formulation introduced in this paper can significantly increase the current scope of application of voxel-based bone models, especially to problems involving contact.

DOI: 10.1002/nme

ACKNOWLEDGEMENTS

The authors would like to acknowledge funding from the Research Fund KU Leuven, Grant STRT1/08/027. DB acknowledges his research stay at KU Leuven was made possible with the support of the Erasmus Mundus programme of the European Union. The assistance of Mr Sujeet Phanse in using the MATLAB function pcg (pre-conditioned conjugate gradients) to solve the very large DOF models is acknowledged.

REFERENCES

1. van Rietbergen B. Micro-FE analyses of bone: state of the art. *Noninvasive Assessment of Trabecular Bone Architecture and the Competence of Bone*, Majumdar S, Bay BK (eds.). Springer US: Boston, MA, 2001; 21–30, doi:10.1007/978-1-4615-0651-5_3.
2. van Rietbergen B, Ito K. A survey of micro-finite element analysis for clinical assessment of bone strength: The first decade. *Journal of Biomechanics* 2015; **48**(5):832–841, doi:10.1016/j.jbiomech.2014.12.024.
3. Wirth AJ, Müller R, van Lenthe GH. Computational analyses of small endosseous implants in osteoporotic bone. *European Cells and Materials* 2010; **20**:58–71.
4. Flaig C, Arbenz P. A scalable memory efficient multigrid solver for micro-finite element analyses based on CT images. *Parallel Computing* 2011; **37**(12):846–854, doi:10.1016/j.parco.2011.08.001.
5. Pistoia W, van Rietbergen B, Lochmüller EM, Lill CA, Eckstein F, Rüegsegger P. Image-based micro-finite-element modeling for improved distal radius strength diagnosis: moving from bench to bedside. *Journal of Clinical Densitometry* 2004; **7**:153–160, doi:10.1385/JCD:7:2:153.
6. Ito M. Assessment of bone quality using micro-computed tomography (micro-CT) and synchrotron micro-CT. *Journal of Bone and Mineral Metabolism* 2005; **23**(1):115–121, doi:10.1007/BF03026335.
7. Colloca M, Blanchard R, Hellmich C, Ito K, van Rietbergen B. A multiscale analytical approach for bone remodeling simulations: Linking scales from collagen to trabeculae. *Bone* 2014; **64**:303–313, doi:10.1016/j.bone.2014.03.050.
8. Wirth AJ, Müller R, van Lenthe GH. The discrete nature of trabecular bone microarchitecture affects implant stability. *Journal of Biomechanics* 2012; **45**:1060–1067, doi:10.1016/j.jbiomech.2011.12.024.
9. Arbenz P, Flaig C. On smoothing surfaces in voxel based finite element analysis of trabecular bone. *6th International Conference on Large-Scale Scientific Computing*, Lirkov I, Margenov S, Waśniewski J (eds.). Springer: Berlin, Heidelberg, 2008; 69–77, doi:10.1007/978-3-540-78827-0.
10. Boyd SK, Müller R. Smooth surface meshing for automated finite element model generation from 3D image data. *Journal of Biomechanics* 2006; **39**:1287–1295, doi:10.1016/j.jbiomech.2005.03.006.

11. Camacho DL, Hopper RH, Lin GM, Myers BS. An improved method for finite element mesh generation of geometrically complex structures with application to the skullbase. *Journal of Biomechanics* 1997; **30**:1067–1070, doi:10.1016/S0021-9290(97)00073-0.

12. Wang ZL, Teo JCM, Chui CK, Ong SH, Yan CH, Wang SC, Wong HK, Teoh SH. Computational biomechanical modelling of the lumbar spine using marching-cubes surface smoothened finite element voxel meshing. *Computer Methods and Programs in Biomedicine* 2005; **80**:25–35, doi:10.1016/j.cmpb.2005.06.006.

13. Guldberg RE, Hollister SJ, Charras GT. The accuracy of digital image-based finite element models. *Journal of Biomechanical Engineering* 1998; **120**:289–295, doi:10.1115/1.2798314.

14. Stadelmann VA, Conway CM, Boyd SK. In vivo monitoring of bone-implant bond strength by microCT and finite element modelling. *Computer Methods in Biomechanics and Biomedical Engineering* 2011; **16**:993–1001, doi: 10.1080/10255842.2011.648625.

15. Steiner JA, Ferguson SJ, van Lenthe GH. Computational analysis of primary implant stability in trabecular bone. *Journal of Biomechanics* 2015; **48**:807–815, doi:10.1016/j.jbiomech.2014.12.008.

16. Wirth AJ, Goldhahn J, Flaig C, Arbenz P, Müller R, van Lenthe GH. Implant stability is affected by local bone microstructural quality. *Bone* 2011; **49**:473–478, doi:10.1016/j.bone.2011.05.001.

17. Hallquist JO, Goudreau GL, Benson DJ. Sliding interfaces with contact-impact in large-scale Lagrangian computations. *Computer Methods in Applied Mechanics and Engineering* 1985; **51**:107–137, doi:10.1016/0045-7825(85)90030-1.

18. Wriggers P. *Computational Contact Mechanics*. Second edn., Springer-Verlag: Berlin, Heidelberg, 2006, doi: 10.1007/978-3-540-32609-0.

19. Timoshenko S, Goodier JN. *Theory of Elasticity*. Second edn., McGraw-Hill Book Company: New York, 1951.

20. Zienkiewicz OC, Taylor RL, Zhu JZ. *The Finite Element Method*. Sixth edn., Butterworth-Heinemann: Oxford, 2005, doi:10.1016/B978-075066431-8.50165-X.

21. Zienkiewicz OC, Taylor RL, Fox D. *The Finite Element Method for Solid and Structural Mechanics*. Seventh edn., Butterworth-Heinemann: Oxford, 2014, doi:10.1016/B978-1-85617-634-7.00016-8.

22. Grosland NM, Brown TD. A voxel-based formulation for contact finite element analysis. *Computer Methods in Biomechanics and Biomedical Engineering* 2002; **5**:21–32, doi:10.1080/10255840290032180.

23. The VAKHUM project public dataset. http://www.ulb.ac.be/project/vakhum/public_dataset/public-data.htm. Accessed: 14 March 2017.

24. Van Sint Jan S. The VAKHUM project: virtual animation of the kinematics of the human. *Theoretical Issues in Ergonomics Science* 2005; **6**(3–4):277–279, doi:10.1080/14639220412331529591.

25. Aitkenhead AH. Mesh voxelisation. http://uk.mathworks.com/matlabcentral/fileexchange/27390-mesh-voxelisation. Accessed: 14 March 2017.

26. Banglawala N. VOX-FE: Finite element modelling of bone. https://www.epcc.ed.ac.uk/projects-portfolio/vox-fe-finite-element-modelling-bone. Accessed: 18 Jan 2018.

27. Adams MF, Bayraktar HH, Keaveny TM, Papadopoulos P. Ultrascalable implicit finite element analyses in solid mechanics with over a half a billion degrees of freedom. *Supercomputing, 2004. Proceedings of the ACM/IEEE SC2004 Conference*, 2004; 34–34, doi:10.1109/SC.2004.62.
28. Pahr DH, Schwiedrzik J, Dall'Ara E, Zysset PK. Clinical versus pre-clinical FE models for vertebral body strength predictions. *Journal of Mechanical Behaviour of Biomedical Materials* 2014; **33**:76–83, doi:10.1016/j.jmbbm.2012.11.018.
29. Folkestad L, Hald JD, Hansen S, Gram J, Langdahl B, Abrahamsen B, Brixen K. Bone geometry, density, and microarchitecture in the distal radius and tibia in adults with osteogenesis imperfecta type I assessed by high-resolution pQCT. *Journal of Bone and Mineral Research* 2012; **27**(6):1405–12, doi:10.1002/jbmr.1592.
30. Enns-Bray WS, Owoc JS, Nishiyama KK, Boyd SK. Mapping anisotropy of the proximal femur for enhanced image based finite element analysis. *Journal of Biomechanics* 2014; **47**(13):3272–8, doi:10.1016/j.jbiomech.2014.08.020.
31. Tsubota Ki, Adachi T, Tomita Y. Effects of a fixation screw on trabecular structural changes in a vertebral body predicted by remodeling simulation. *Annals of Biomedical Engineering* 2003; **31**(6):733–740, doi:10.1114/1.1574028.
32. Costa MC, Tozzi G, Cristofolini L, Danesi V, Viceconti M, Dall'Ara E. Micro finite element models of the vertebral body: Validation of local displacement predictions. *PLoS One* 2017; **12**(7):e0180 151, doi:10.1371/journal.pone.0180151.
33. Mueller TL, Stauber M, Kohler T, Eckstein F, Muller R, van Lenthe GH. Non-invasive bone competence analysis by high-resolution pQCT: an in vitro reproducibility study on structural and mechanical properties at the human radius. *Bone* 2009; **44**(2):364–71, doi:10.1016/j.bone.2008.10.045.
34. Nawathe S, Akhlaghpour H, Bouxsein ML, Keaveny TM. Microstructural failure mechanisms in the human proximal femur for sideways fall loading. *Journal of Bone and Mineral Research* 2014; **29**(2):507–15, doi:10.1002/jbmr.2033.
35. Eckstein F, Matsuura M, Kuhn V, Priemel M, Muller R, Link TM, Lochmuller EM. Sex differences of human trabecular bone microstructure in aging are site-dependent. *Journal of Bone and Mineral Research* 2007; **22**(6):817–24, doi:10.1359/jbmr.070301.
36. Makela JT, Huttu MR, Korhonen RK. Structure-function relationships in osteoarthritic human hip joint articular cartilage. *Osteoarthritis and Cartilage* 2012; **20**(11):1268–77, doi:10.1016/j.joca.2012.07.016.
37. Armstrong CG, Gardner DL. Thickness and distribution of human femoral head articular cartilage. changes with age. *Annals of the Rheumatic Diseases* 1977; **36**(5):407–12.
38. Lorensen WE, Cline HE. Marching cubes: A high resolution 3d surface construction algorithm. *SIGGRAPH '87 Proceedings of the 14th annual conference on Computer graphics and interactive techniques*, vol. 21, 1987; 163–69, doi:10.1145/37401.37422.

Table I. Coordinates of the locations shown in Figure 1A.

	Loc-1	Loc-2	Loc-3	Loc-4	Loc-5	Loc-6	Loc-7
X/R	1.000	0.577	0.707	0.924	0.888	0.674	0.855
Y/R	0.000	0.577	0.000	0.000	0.325	0.303	0.216
Z/R	0.000	0.577	0.707	0.383	0.325	0.674	0.472

DOI: 10.1002/nme

Table II. Comparison of normalized maximum absolute error (NMAXABSE) and normalized root mean squared error (NRMSE) in principal (σ_1, σ_2, σ_3), normal (σ_{xx}, σ_{yy}, σ_{zz}) and shear (σ_{xy}, σ_{xz}, σ_{yz}) stress fields for the bonded, stair-case, sliding contact (SC-SC) and simulated smoothed surface, sliding contact (SS-SC) formulations compared to the benchmark model of femur–acetabulum contact.

	NMAXABSE			NRMSE		
	Bonded	SC-SC	SS-SC	Bonded	SC-SC	SS-SC
σ_1	0.943	0.510	0.560	0.116	0.0291	0.00853
σ_2	0.941	0.540	0.511	0.153	0.0336	0.00817
σ_3	1.75	0.676	0.427	0.305	0.0409	0.00806
σ_{xx}	1.45	0.433	0.440	0.260	0.0387	0.00728
σ_{yy}	0.957	0.429	0.387	0.116	0.0290	0.00689
σ_{zz}	1.60	0.839	0.444	0.213	0.0299	0.00829
σ_{xy}	2.31	0.894	0.354	0.266	0.0436	0.00925
σ_{xz}	2.75	0.700	0.285	0.422	0.0473	0.0102
σ_{yz}	1.78	1.01	0.450	0.217	0.0496	0.0116

DOI: 10.1002/nme

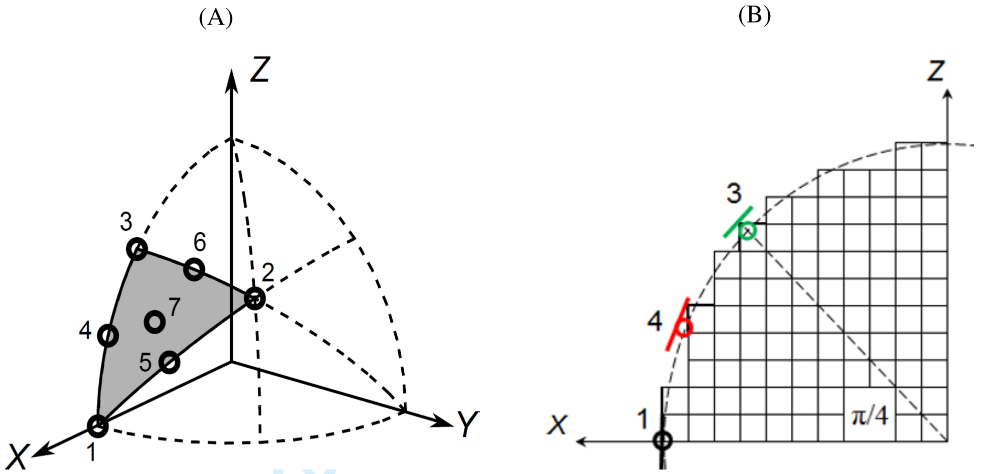

Figure 1. (A) The shaded triangular region is the smallest region on the spherical surface that presents unique orientations of the voxels to a local tangent plane. Seven locations on this shaded region are labeled Loc-1 to Loc-7. Dashed curves lie on symmetry planes about which the shaded region can be repeatedly reflected to recover the entire spherical surface. (B) Reflective symmetry can be visualized on the positive quadrant of the X-Z plane. Unique orientations of the voxels (solid outline) with respect to local tangents (coloured lines) are present entirely within the 45°-sector bounded by the locations Loc-1 and Loc-3.

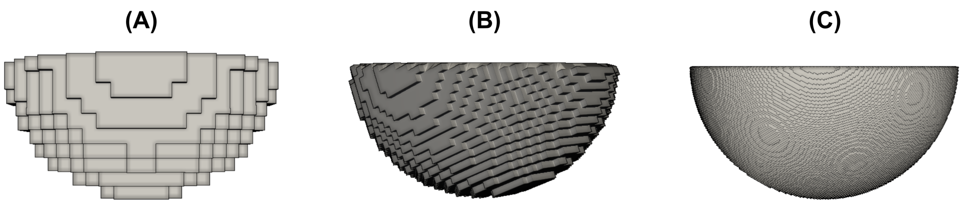

Figure 2. Mesh of the voxelated hemisphere for representative combinations of mesh-refinement and voxel orientation: (A) $a/R = 0.1$ and Loc-1, (B) $a/R = 0.05$ and Loc-4, (C) $a/R = 0.01$ and Loc-7.

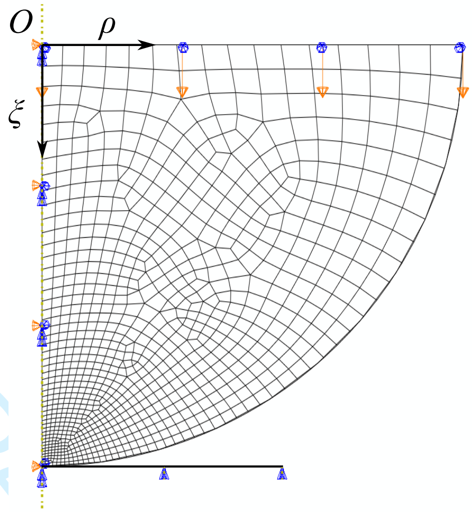

Figure 3. Mesh and applied boundary conditions for the benchmark model.

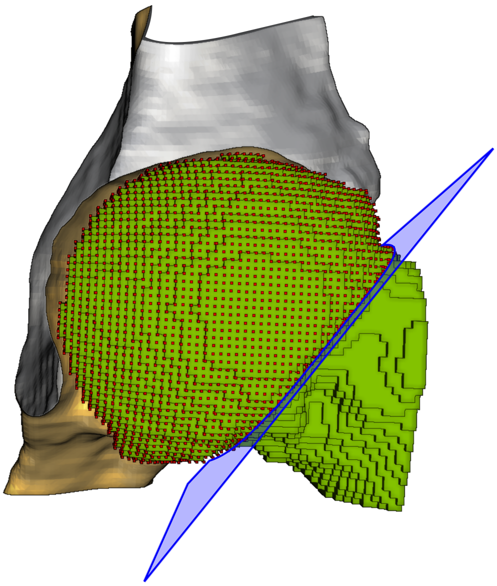

Figure 4. In the voxel models, contact interaction was defined between the outward pelvis surface facets (yellow) and the exterior nodes of the femur (red dots) that were on the acetabulum facing side of a specified plane (transparent blue). Here the pelvis is cut at a coronal cross-section to clarify the position of the acetabular surface with respect to the femoral head in the reference configuration.

DOI: 10.1002/nme

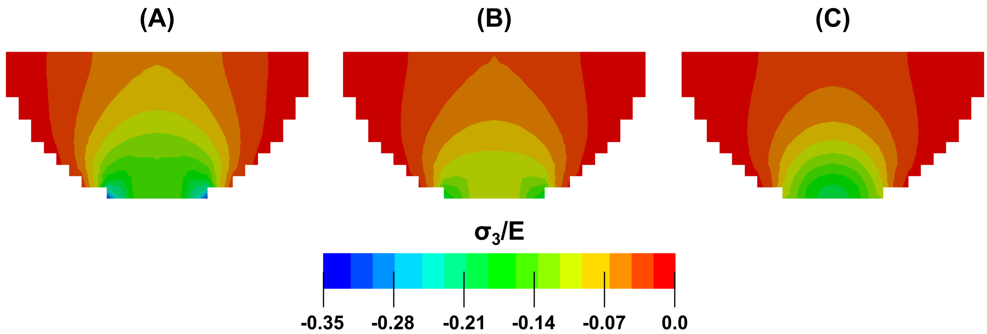

Figure 5. Contours of minimum principal stress computed by (A) bonded, (B) stair-case, sliding contact (SC-SC) and (C) simulated smoothed surface, sliding contact (SS-SC) models, respectively, are shown on the $y = 0$ plane of the hemispheres in the reference configuration, corresponding to $a/R = 0.075$ and Loc-1 case. Stress values are normalized with respect to the Young's modulus E.

DOI: 10.1002/nme

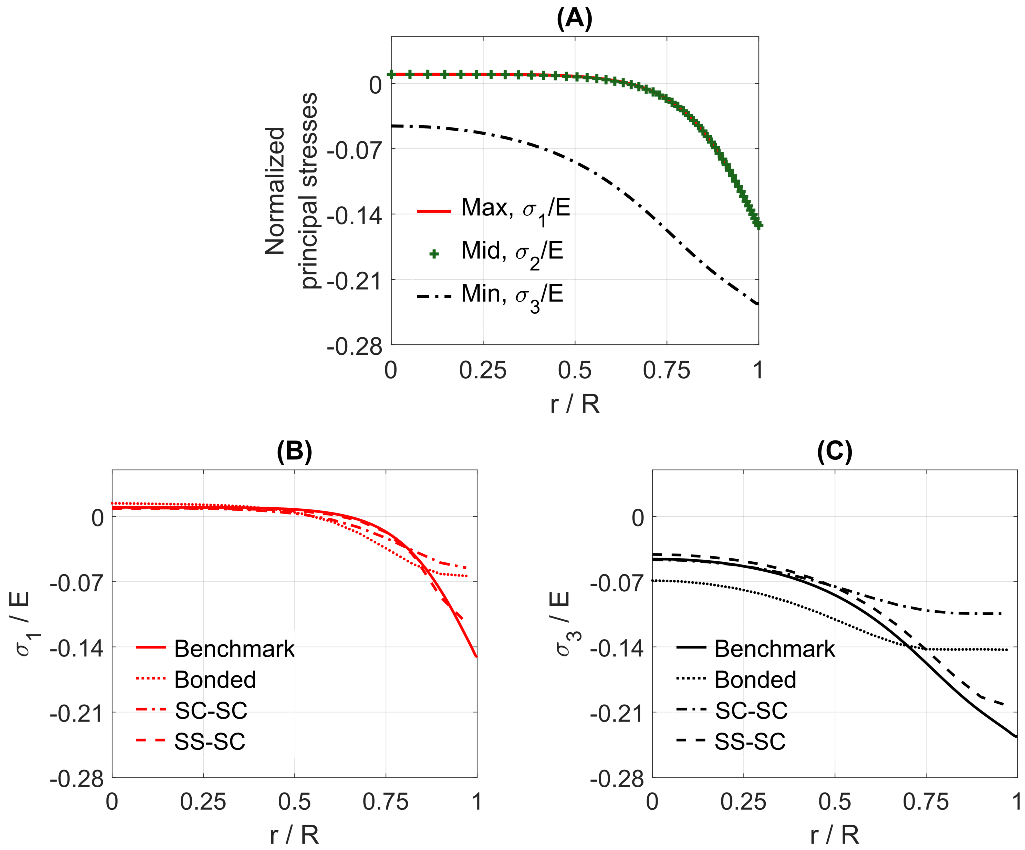

Figure 6. Principal stresses normalized with respect to Young's modulus E along the radial line passing through the point of initial contact. Normalized distances 0 and 1 correspond to the centre of the sphere and the point of initial contact, respectively. (A) Maximum, middle and minimum principal stresses in the benchmark model. For the voxel geometry corresponding to $a/R = 0.075$ and Loc-1, (B) maximum and (C) minimum principal stresses are compared with the benchmark for the bonded, stair-case, sliding contact (SC-SC) and simulated smoothed surface, sliding contact (SS-SC) models.

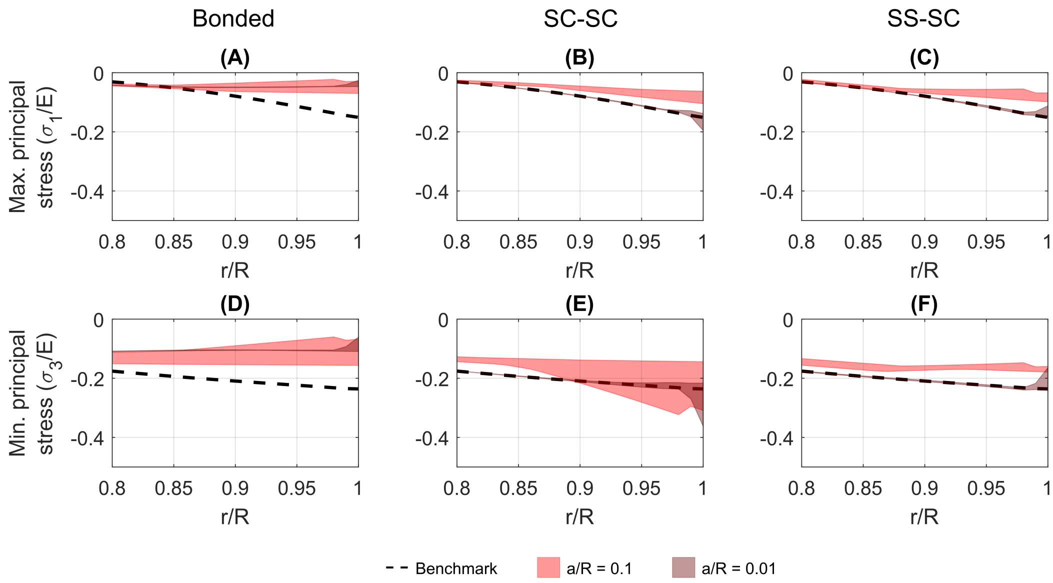

Figure 7. The influence of mesh refinement on the dispersion in predicted stresses across different voxel orientations for the bonded, stair-case, sliding contact (SC-SC) and simulated smoothed surface, sliding contact (SS-SC) models. Predicted stresses for the coarsest ($a/R = 0.1$) and the most refined ($a/R = 0.01$) voxel models are shown. Stresses are normalized with respect to Young's modulus E and plotted along the undeformed radial line and in the region close to contact ($x \geq 0.8$). The shaded envelopes show the dispersion of predicted stresses across the different orientations. The dashed line is the stress predicted by the benchmark model.

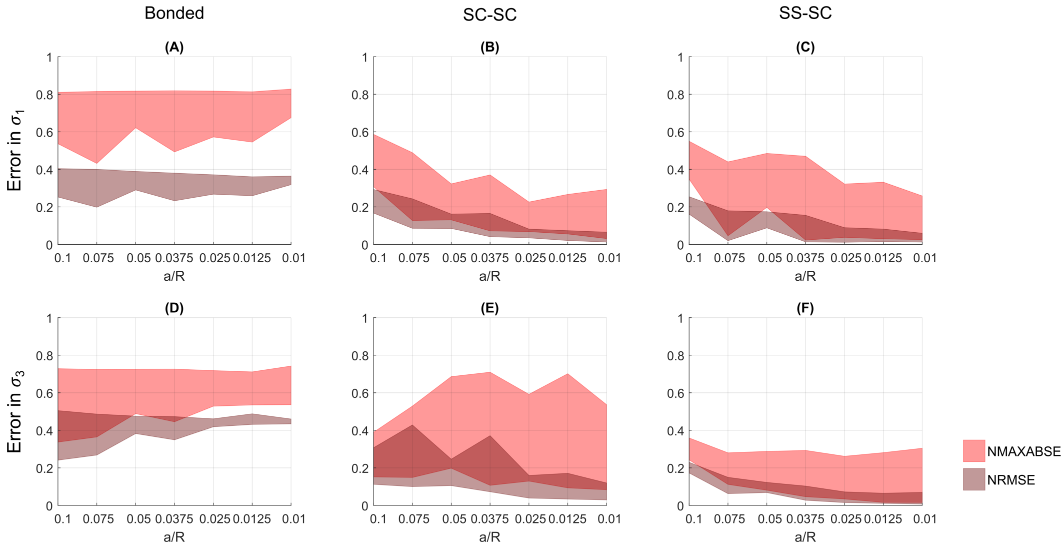

Figure 8. Comparison of normalized maximum absolute error (NMAXABSE) and normalized root mean squared error (NRMSE) in (A–C) maximum and (D–F) minimum principal stress predictions for the bonded, stair-case, sliding contact (SC-SC) and simulated smoothed surface, sliding contact (SS-SC) models. The shaded envelopes depict the dispersion of the errors across the different orientations over a range of mesh refinements.

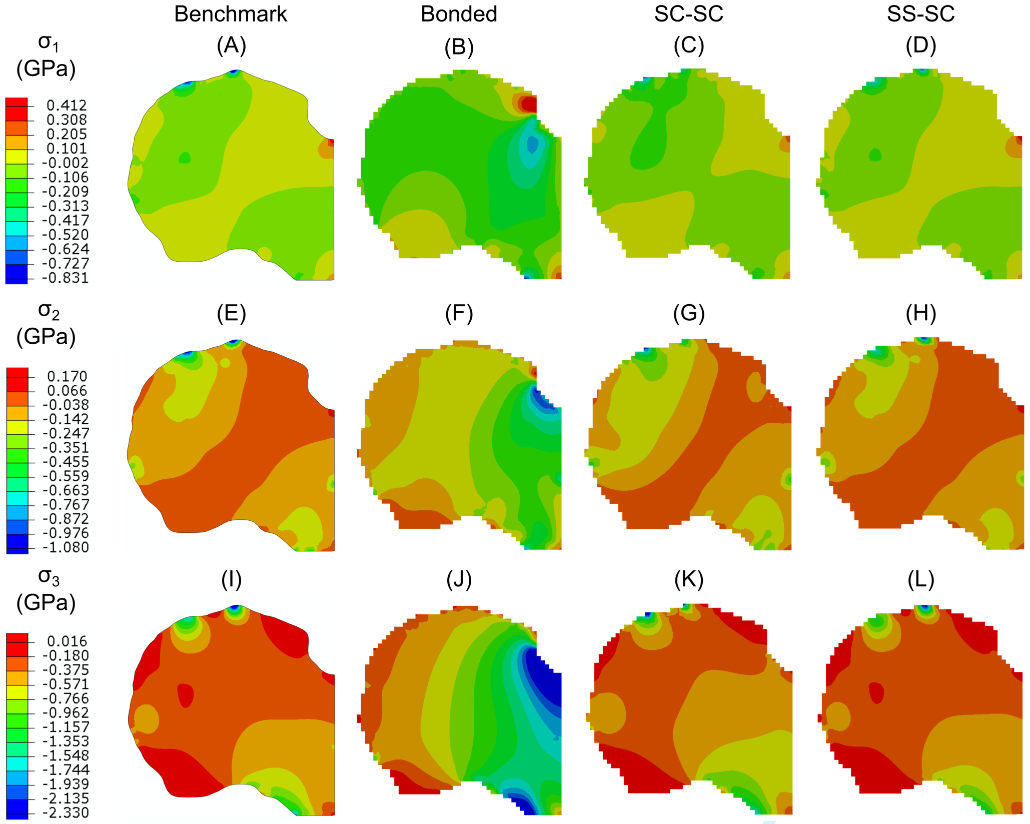

Figure 9. Comparison of principal stresses at the same coronal section between the tetrahedral mesh model (A,E,I) and the voxel mesh models with bonded contact (B,F,J), stair-case, sliding contact or SC-SC (C,G,K) and simulated smoothed surface, sliding contact or SS-SC (D,H,L) formulations.

DOI: 10.1002/nme

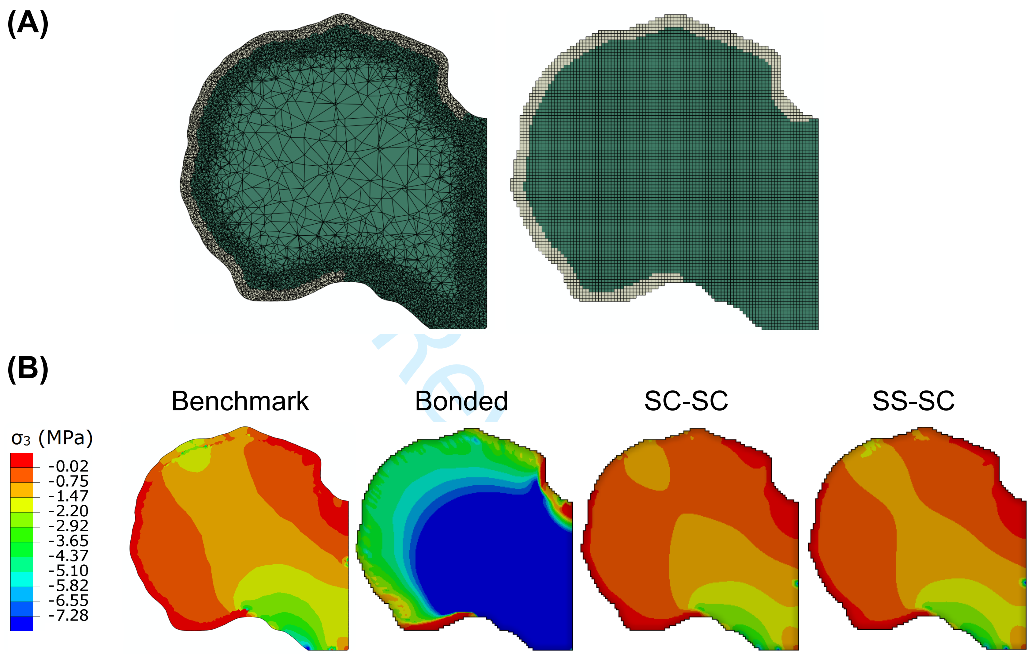

Figure 10. (A) Tetrahedral benchmark (left) and voxel (right) mesh models of the hip with a 2 mm cartilage layer (bright regions) defined on the surface. The green regions are bone. (B) Comparison of minimum principal stresses at the same coronal section between the tetrahedral mesh model and the voxel mesh models with bonded contact, stair-case, sliding contact or SC-SC and simulated smoothed surface, sliding contact or SS-SC formulations.